

Electronic Supplementary Information to:

## Dehydrogenation of undoped sodium alanate at the mechanical interface under room temperature

Esmeralda Muñoz-Cortés,<sup>a</sup> Olga L. Ibryaeva,<sup>b</sup> Miguel Manso,<sup>c</sup> Borja Zabala,<sup>d</sup> Eduardo Flores,<sup>e</sup> Almudena Gutiérrez,<sup>f</sup> Jose Ramon Ares<sup>a</sup> and Roman Nevshupa<sup>f\*</sup>

### 1. Structural characterization of as-received NaAlH<sub>4</sub> powder

X-ray diffraction with Cu K $\alpha$  ( $\lambda = 0.15418$  nm) radiation was employed for structural characterization. The results are shown in Fig. S1.

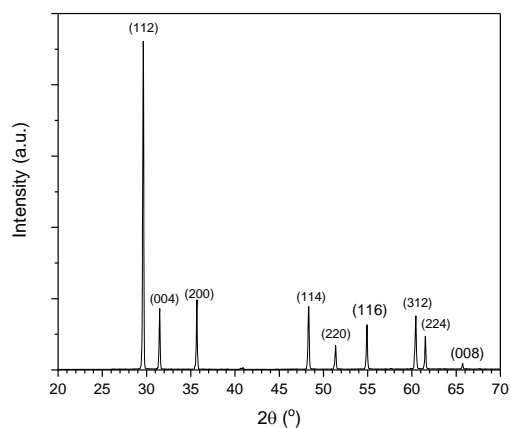


Fig. S1.  $\theta$ -2 $\theta$ X-ray diffraction spectrum of as-received NaAlH<sub>4</sub>. The crystal planes were identified according to literature (shown by numbers at the peaks) <sup>1</sup>.

### 2. Assignment of the signals of TPD-MS to possible ions

Three behaviour patterns were found for the trace gases, namely  $\alpha$  (the group X in Fig. S2 b),  $\beta$  (signals at  $m/z$  15 and 16), and mixed  $\alpha + \beta$  (two groups Y and Z). None of them correlated with the  $\eta$ . The trace gases were tentatively assigned to the products, which could be formed on the surface of NaAlH<sub>4</sub> upon brief exposure to the air during its loading to the TPD-MS since NaAlH<sub>4</sub> is extremely reactive towards O<sub>2</sub>, H<sub>2</sub>O, CO<sub>2</sub>.<sup>2</sup> The pattern  $\beta$  was assigned to CH<sub>4</sub><sup>+</sup>/O<sup>+</sup> and CH<sub>3</sub><sup>+</sup>.

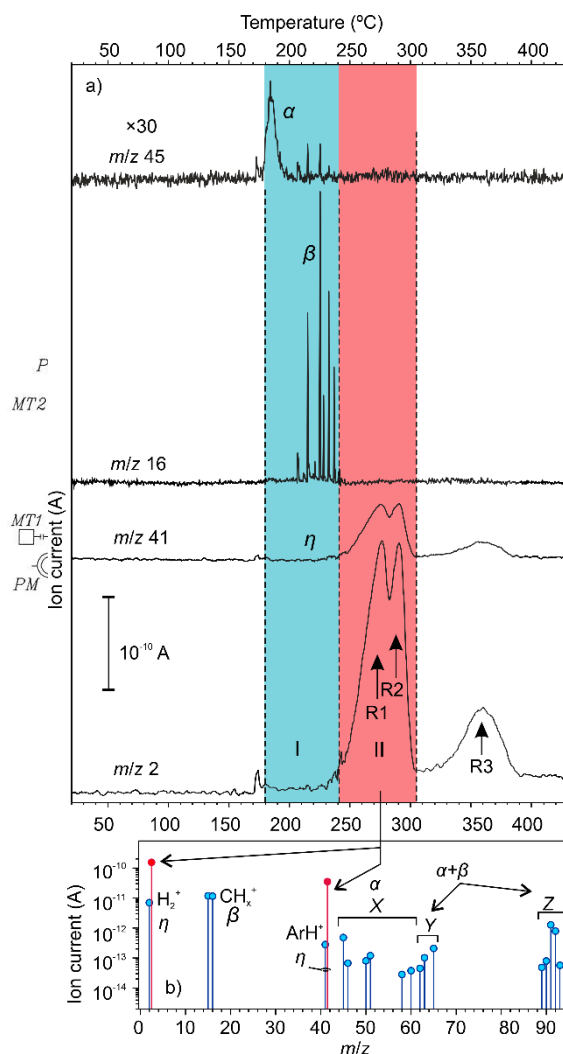


Figure S2. a) Series of various mass-spectrometer signals with increasing temperature, which show typical behaviour patterns denoted by Greek letters; region I corresponds to the initial stage after melting ( $T = 180 - 240$  °C); region II corresponds to the main stage at which H<sub>2</sub> emission occurs via reactions R1 and R2 ( $T = 240 - 305$  °C); b) mean mass-spectra of emitted gases in the stages I (blue open circles) and II (pink filled circles).

<sup>a</sup> Department of Physics of Materials, Autonomía University of Madrid, Spain.

<sup>b</sup> Department of System Programming, South Ural State University, Chelyabinsk, Russia.

<sup>c</sup> Department of Applied Physics, Nicolás Cabrera Institute and Centre for Microanalysis of Materials, Autonomía University of Madrid, Spain.

<sup>d</sup> Tribology unit, Fundación Tekniker, Eibar, Spain.

<sup>e</sup> Departamento de Física Aplicada, Centro de Investigación y de Estudios Avanzados (CINVESTAV), 97310, Mérida, México.

<sup>f</sup> Spanish National Research Council, Eduardo Torroja Institute of Construction Sciences (IETCC-CSIC), Madrid, Spain.

The pattern  $\alpha$  might include partly-oxidized aluminium hydride ( $\text{AlH}_2(\text{OH})$ ,  $\text{AlH}(\text{OH})_2$ ). The groups Y and Z can be related to methyl-substituted alane/sodium alanate or its partly oxidized products.

### 3. Mechanically Stimulated Gas Emission Mass-Spectrometry

A schematic drawing of the experimental ultra-high vacuum system used for characterization of gas emission using operando Mechanically Stimulated Gas Emission Mass-Spectrometry is shown in Fig. S3.

The following describes some results, which are not central to the matter under discussion, but can be helpful to understand the complex mechanochemical processes occurring at sliding interfaces.

Apart from  $\text{H}_2$  and trace gases described in the paper trace water desorption was observed in several cases. The rate of water desorption significantly varied between samples. Therefore, we associated water desorption to with small variations in the sample surface composition, which can be resulted from minor variations in the environment during the storage under a protective atmosphere in the glove box or during the transfer of the samples from the glove box to the experimental vacuum system.

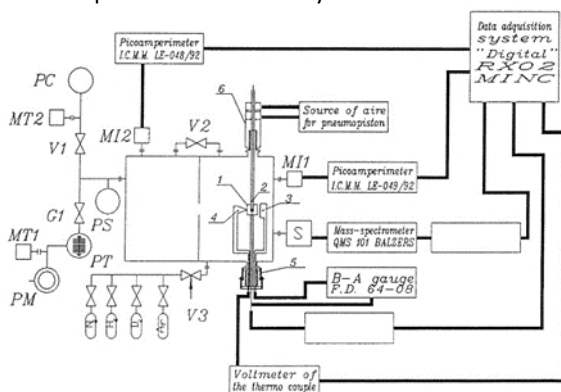


Fig. S3. Schematic layout of the friction system: PC, cryopump; MT2, conductivity gauge to control the pressure in the cryopump; V1, all-metal gate valve to isolate the cryopump; G1, all-metal valve to isolate the turbomolecular pump; PT, turbomolecular pump; MT1, conductivity gauge to control the turbomolecular pump; PM mechanical pump; N<sub>2</sub>... Ar, gas bottles; V3, leak valve; PS, titanium sublimation pump; MI2, ion gauge of chamber 2; MI1, ion gauge of chamber 1, friction chamber; S, quadrupole mass spectrometer; (5), Sample holder with load device and feedthrough; (6), Linear motion device; V2, bypass valve; (1, 2, 3, 4), sample, thermocouple, indenter and filament for electron bombardment of the sample. (Reprinted from Ref. <sup>3</sup>, Copyright 1999, with permission from Elsevier).

Water can be formed on the surface due to oxidation of  $\text{NaAlH}_4$  by residual adsorbed oxygen or decomposition of residual hydroxides. Since such reactions are of less importance for the main

dehydrogenation process, the analysis of water desorption was considered out of the scope of the current work (although of relevance for future studies on the final energy conversion efficiency). The component of a mass spectrum at  $m/z = 44$  can be assigned to  $\text{CO}_2$  which is a product of mechanical decomposition of residual sodium carbonate being a product of  $\text{NaAlH}_4$  reaction with atmospheric  $\text{CO}_2$ .<sup>4,5</sup>

The ions at  $m/z = 66$  and  $100 - 104$  can be tentatively assigned to partly methyl-substituted alanes and alanate<sup>6</sup>, which could be formed on the sample surfaces due to mechanochemical reactions with carbonaceous airborne contaminations, though further study is needed to confirm such reactions.

The correlations between various mass-spectrometric signals are shown in Fig. S4. The loops are indicative of the time lag between emissions of various components. For example, the clockwise loop such as in Fig. S4 a means that the emission of precursors of ions with  $m/z = 89$  anticipated the emission of precursors of ions with  $m/z = 29$ . The counter-clockwise loops (Fig. S4 b) mean that the signals shown in the graph fall behind the reference signal denoted at the abscissa axis.

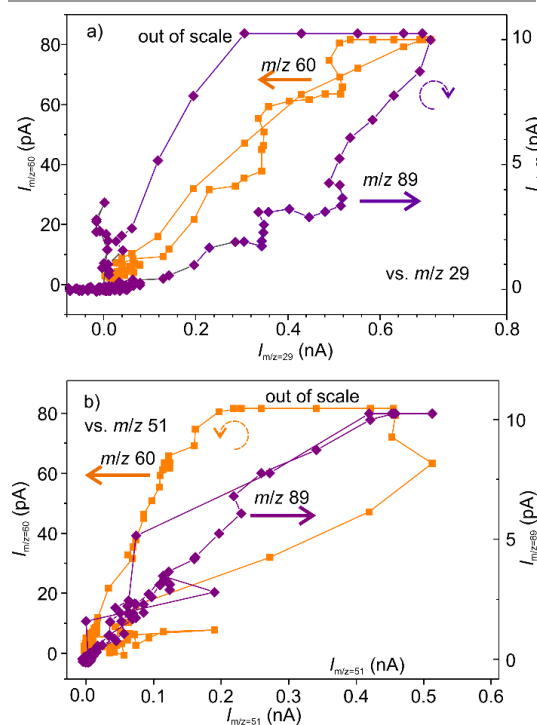


Figure S4. Correlation analysis of mass-spectrometric signals a)  $m/z$  60 and 89 vs.  $m/z$  29; b)  $m/z$  60 and 89 vs.  $m/z$  51. The dashed arrows show the directions of the evolution of the signals with time in the corresponding loops.

From the standpoint of the linked diffusion-wear model of tribo-induced dehydrogenation of  $\text{NaAlH}_4$ , which was put forward in this paper, the

delayed emission can be related to the emission sources situating deeper in the bulk, while the anticipated emission is associated with more superficial emission sources.

#### 4. Mu-FTIR

Figure S5 shows the FTIR absorption spectra measured on pristine and worn surfaces of the pellet.

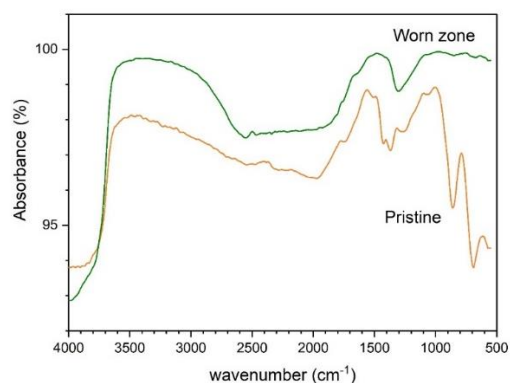


Fig. S5. FTIR absorbance spectra for mechanically affected (worn) and pristine surfaces of NaAlH<sub>4</sub> pellets.

#### 5. The use of Matrix Pencil Method for the analysis of time series

To estimate the number of exponential decays and their parameters during both oscillatory and retarded stages the Matrix Pencil Method (MPM) was employed.<sup>7</sup> This method is less sensitive to noise than Prony-like methods due to Singular Value Decomposition and fewer computational operations. It needs fewer number of operations than Prony method and hence lower computational error. The poles correspond to the time constants of exponential decays,  $\tau_{s,i}$ , which best fit the empirical data during each oscillatory cycle. Only one pole could be reliably determined during each cycle because of the limited cycle period (1 s).

#### 6. Analysis of reaction order behind “trail” hydrogen emission

The slow emission decay, which does not obey a first-order reaction (exponential), can be generally due to one of the two reasons: 1) the reaction order is not first, 2) there are several parallel first-order processes with different kinetics contributing to the total emission. The following analysis was carried out to check whether the experimental data fit the kinetic equation of the reactions of any order different from first. Table S1 shows the kinetic equations of reactions of various orders.<sup>8</sup>

Reaction order	Reaction rate	Integrated equation (A=f(t))
0	$k$	$[A]=[A_0] - kat^a$
1	$k[A]$	$\ln [A]=\ln [A_0] - kat$
2	$k[A]^2$	$\frac{1}{[A]} = \frac{1}{[A_0]} + kat$
3	$k[A]^3$	$\frac{1}{[A]^2} = \frac{1}{[A_0]^2} + 2kat$
$n$	$k[A]^n$	$[A]^{1-n}=[A_0]^{1-n} + (n-1)kat$

Table S1. Reaction orders with their corresponding equations

<sup>a)</sup>  $a$  is the stoichiometric coefficient,  $t$  is the time,  $A$  is the reagent concentration,  $A_0$  is the initial concentration,  $n$  is the reaction order

The hypothesis that the data obeys a reaction with a certain order is accepted if the experimental data can be fitted by the corresponding function. For the sake of simplicity, the experimental data can be transformed in such a way that the relationship between the transformed data and time is linear. Then, the hypothesis test is conducted by a simple linear fitting procedure. Therefore, a practical method was carried out on the basis of the integrated equations and their corresponding graphs shown in Fig. S6, where  $t$  is the time. The goodness of fit was evaluated from the adjusted coefficient of determination,  $R_{adj}$ .<sup>2</sup> Table S2 shows the obtained values of  $R_{adj}$ .<sup>2</sup> The experimental data were best fitted by the first-order equation. Although there is a deviation from linearity, it is clear that the experimental data combines various straight lines that is indicative of multiple parallel first-order reactions. The parameters of each first-order processes can be determined using piece-wise

linear fitting or Method of Pencil Matrixes. The goodness of fit for the second-order reaction is quite high, but the data presented significant deviation from linearity that was the reason to decline this hypothesis.

On the basis of this modelling it was concluded that the emission decay must be a combination of several first-order processes of different kinetics.

Table S2. Linear correlation coefficients

Order	$R_{adj.}^2$
0	0.9614
<b>1</b>	<b>0.9771</b>
2	0.7649
3	0.8296

Similar results were obtained using the method of half times.

## 7. Analysis of the hypotheses of hydrogen emission

### 7.1. The hypothesis of generation of nanoparticles by rubbing

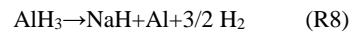
If nanoparticles are generated by rubbing, the time constant of mechanically stimulated dehydrogenation will depend on the particles' size distribution according to the Arrhenius-type first-order equation proposed by Baldé et al.<sup>9</sup>

$$\tau_{np} = (k_d \exp(-E_{a,d}(d_{np})/RT))^{-1}, \text{ (ESI 1)}$$

where  $k_d$  is the pre-exponential factor,  $E_{a,d}$  is the activation energy for dehydrogenation,  $d_{np}$  is the particle size,  $R$  is universal gas constant and  $T$  is the temperature. The activation energy increases from 58 kJ/mol to 80 kJ/mol as the particle size increases from 2 - 10 nm to 19 - 30 nm.<sup>9</sup> Taking the following values of parameters:<sup>10</sup>  $k_d = 1.07 \times 10^9 \text{ s}^{-1}$ ,  $d_{np} = 2 - 10 \text{ nm}$ ,  $E_{a,d} = 58 \text{ kJ/mol}$ ,  $R = 8.31 \text{ J/(mol K)}$ , and  $T = 300 \text{ K}$  the  $\tau_{np} = 11.9 \text{ s}$  was obtained. This is quite close to the second empirical time constants  $\tau^s_2$  and  $\tau^m_2$ . In this perspective, it is reasonable to suggest that the  $\tau^s_1$  and  $\tau^s_3$  correspond to nanoparticles with  $d_{np} < 2 \text{ nm}$  and  $10 < d_{np} < 19 \text{ nm}$ , respectively. For instance,  $\tau^s_1 = 0.6 \text{ s}$  and  $\tau^s_3 = 306 - 465 \text{ s}$  will require  $E_{a,d} = 50 - 51 \text{ kJ/mol}$  and  $E_{a,d} = 66.1 - 67.1 \text{ kJ/mol}$ , correspondingly.

Formation of nanoparticles under mechanical abrasion cannot be discarded fully. We added an enlarged SEM image (Fig. 9 i) of a portion of the surface zone where various submicrometer particles in the range of several hundreds of nanometers can be seen. Considering how difficult the manufacturing of nanoparticles is by high energy milling and based on our previous experience on studying nanoparticle aerosol generation, it is not reasonable to consider that a significant volume of mechanically affected material was transformed into ultrafine nanoparticles. Furthermore, our experimental results showed that the dominating portion of emitted gases are released with fast kinetics, which means that, if the hydrogen release is due to the formation of nanoparticles, the nanoparticles have to have a size below 30 nm, which supposition has not been supported by SEM. Therefore, we do not believe that the formation of nanoparticles can be the dominating mechanism of dehydrogenation under given experimental conditions. Further studies can be useful to understand the contribution of this mechanism to the total hydrogen release.

### 7.2. The hypothesis of two-step reaction pathway R5 & R8



The effect of stress,  $\sigma$ , on the reaction rate,  $r$ , is expressed as following:<sup>11</sup>

$$r = k \exp\left(-\frac{E_a - \sigma V_a}{RT}\right), \text{ (ESI 2)}$$

where  $k$  is the pre-exponential factor,  $E_a$  is the activation energy and  $V_a$  is the activation volume. Taking the following values of parameters:  $E_a = 116 \text{ kJ/mol}$   $\text{AlH}_3$  and  $V_a = 10 \text{ \AA}^3/\text{bond} \times 6.02 \times 10^{23} \text{ bonds/mol}$ , and accepting the value of hardness as the upper limit of  $\sigma = 0.7 - 10 \text{ MPa}$ <sup>12</sup> it was obtained that  $\sigma V_a = 4.2 - 60 \text{ J/mol}$  or  $< 0.05 \%$  of  $E_a$ .

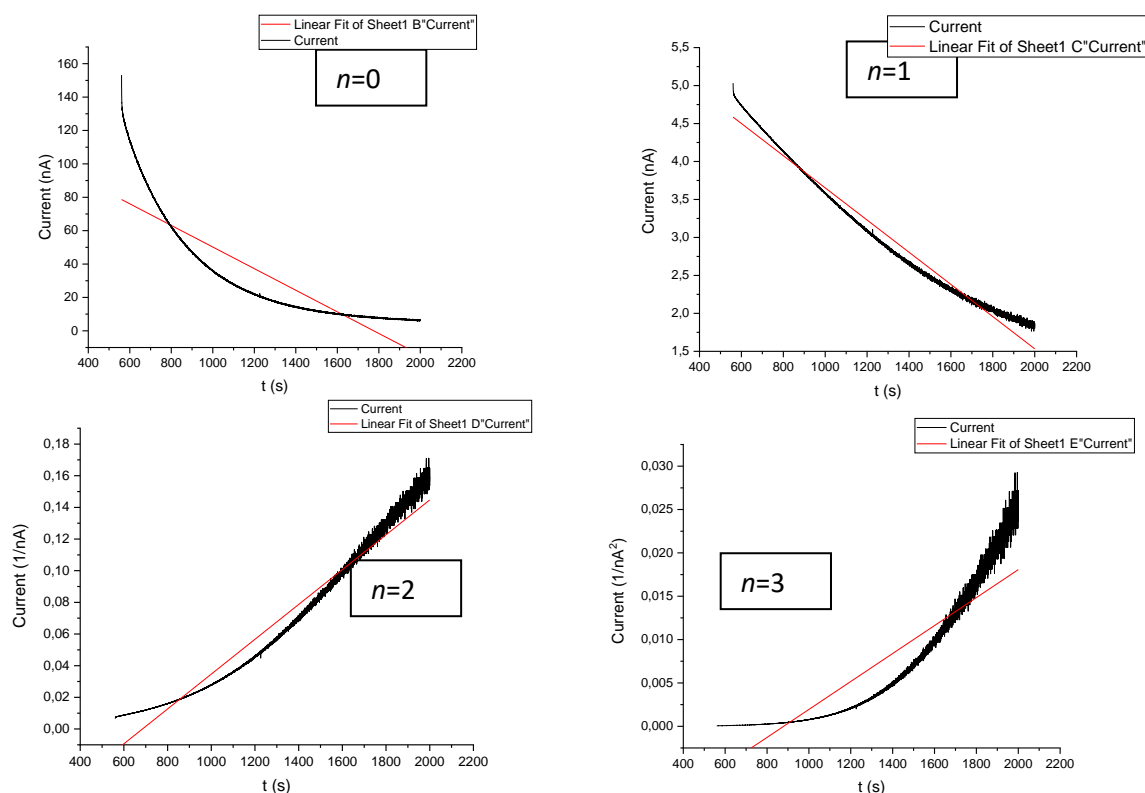


Figure S6. Fitting transformed experimental data by linear functions in order to determine the reaction order responsible for retarded hydrogen emission: a) zero order, b) first order, c) second order, d) third order.

## References

1. K. J. Gross, G. Sandrock and G. J. Thomas, *Journal of Alloys and Compounds*, 2002, **330-332**, 691-695.
2. M. H. W. Verkuijlen, R. de Gelder, P. J. M. van Bentum and A. P. M. Kentgens, *The Journal of Physical Chemistry C*, 2011, **115**, 7002-7011.
3. R. A. Nevchoupa, J. L. De Segovia and E. A. Deulin, *Vacuum*, 1999, **52**, 73-81.
4. R. B. Daniel E. Dedrick, Jr., and Robert W. Bradshaw *The reactivity of sodium alanates with O<sub>2</sub>, H<sub>2</sub>O, and CO<sub>2</sub>*, Report SAND2007-4960, Sandia National Laboratories, Albuquerque, USA, 2007.
5. F. Urakaev, *Physics and Chemistry of Minerals*, 2007, **34**, 351-361.
6. Y. S. Hiraoka and M. Mashita, *Journal of Crystal Growth*, 1994, **145**, 473-477.
7. M. P. Henry, O. L. Ibryaeva, D. D. Salov and A. S. Semenov, *Bulletin of the South Ural State University. Series "Mathematical Modelling, Programming and Computer Software"*, 2017, **10**, 92-104.
8. R. G. Mortimer, *Physical Chemistry*, Harcourt/Academic Press 2000.
9. C. Baldé, *Sodium alanate nanoparticles for hydrogen storage*, Utrecht University, Utrecht, 2008.
10. G. Sandrock, K. Gross and G. Thomas, *Journal of Alloys and Compounds*, 2002, **339**, 299-308.
11. V. R. Regel', A. I. Slutsker and É. E. Tomashevskii, *Uspekhi Fizicheskikh Nauk*, 1972, **106**, 193-228.
12. A. Boscoboinik, D. Olson, H. Adams, N. Hopper and W. T. Tysoe, *Chemical Communications*, 2020, **56**, 7730-7733.